Chemically Linked Metal-Matrix Nanocomposites of Boron Nitride Nanosheets and Silver as Thermal Interface Materials

N. Nagabandi[1], C. Yegin[2], X. Feng[3], C. King[3], J.K. Oh[2], E.A. Scholar[4], S. Narumanchi[3], M. Akbulut[1, 2, 4]*

[1]Artie McFerrin Department of Chemical Engineering, Texas A&M University, College Station, TX 77843-3122, USA

[2]Department of Materials Science and Engineering, Texas A&M University, College Station, TX 77843-3003, USA

[3]National Renewable Energy Laboratory (NREL), 15013 Denver West Parkway, Golden, CO 80401, USA

[4]Texas A&M Energy Institute, Texas A&M University, 3372 TAMU, College Station, TX 77843-3372, USA

Abstract

Herein, novel hybrid nanocomposite thermal interface materials (TIMs) relying on the chemical linkage of silver, boron nitride nanosheets (BNNSs), and organic ligands are reported. These TIMs were prepared using a co-electrodeposition/chemisorption approach where the electrolytic reduction of silver ions into silver nano-/micro-crystals was coupled with the conjugation of ligand-coated nanosheets onto silver crystals. Furthermore, the influence of bond strength of silver/nanosheet links on the thermal, mechanical, and structural properties is investigated using a combination of techniques including laser flash analysis, phase-sensitive transient thermoreflectance, nanoindentation, and electron microscopy. Internal nanostructure was found to be strongly dependent on the linker chemistry. While the chemical grafting of 4-cyano-benzoyl chloride (CBC) and 2-mercapto-5-benzimidazole carboxylic acid (MBCA) on BNNSs led to the uniform distribution of functionalized-nanosheets in the silver crystal matrix, the physical binding of 4-bromo-benzoyl chloride (BBC) linkers on nanosheets caused the aggregation and phase separation. The thermal conductivity was 236-258 W/m-K and 306-321 W/m-K for physically and chemically conjugated TIMs, respectively, while their hardness varied from 495 to 400 MPa and from 240 to 360 MPa, respectively. The corresponding ratio of thermal conductivity to hardness, which is a critical parameter controlling the performance of TIMs, was ultrahigh for the chemically conjugated TIMs: 1.3×10^{-6} m^2/K-s for MBCA-BNNS and 8.5×10^{-7} m^2/K-s for CBC-BNNS. We anticipate that these materials can satisfy some of the emerging thermal management needs arising from the improved performance and efficiency, miniaturization, and/or high throughput of electronic devices, energy storage devices, energy conversion systems, light-emitting diodes, and telecommunication components.

KEYWORDS: Thermal management, 2-D nanomaterials, Nanostructured materials, Nanocomposites

1. Introduction

Thermal management is a multidisciplinary field which is getting increasing attention in various applications, including processors, electronic devices, power storage devices, power inverters and converters, light-emitting diodes, and telecommunication systems [1-12]. This trend is primarily driven by recent technological developments leading to smaller but more powerful processors and electronic devices, larger energy density in energy storage devices, and higher speed and frequency operation of moving components of machinery. A typical approach to thermal management is to reduce the thermal contact resistance between a heat source to a heat sink by filling interstitial gaps with soft, conformal, high thermal conductivity materials, which are often referred as thermal interface materials (TIMs) [13-18].

The thermal contact resistance, *R*, is one of the major factors limiting the rate at which heat can be dissipated from engineered devices, components, and systems having a finite surface roughness [19, 20]. According to the theoretical models [21, 22], the contact conductance, *1/R*, can be expressed as:

$$1/R = 1.25k\, m/\sigma * (P/H)^{0.95} \quad [1]$$

where *k* is the harmonic mean thermal conductivity of the contacting surfaces, m is the effective absolute surface slope, σ is the effective rms roughness, P is the contact pressure, and H is the micro-hardness of the softer material. From a perspective of the material property design, to minimize the thermal contact resistance, as a first approximation, one needs to maximize the ratio of thermal conductivity to hardness. In addition, since the operation of TIMs involves the exposure to on/off and heating/cooling cycles, the thermal stresses induced at the interface of heat

sink/TIM/heat source strongly depends on the elastic modulus, i.e. a soft and compliant materials are desired to minimize thermal stresses at the interface. Considering these points, various strategies have been explored and implemented. For instance, there are numerous publications in the literature reporting the incorporation of high thermal conductivity fillers such as silver particles, copper particles, graphene, carbon nanotubes, and silicon carbide and diamond powder into a soft, compliant polymer matrix or viscous oil to form polymer pads, thermal greases, and thermal compounds [23-30]. For these types of materials, the current state-of-art in the ratio of thermal conductivity to hardness lies in the range of 2×10^{-9} to 10×10^{-9} m^2/K-s.

An alternative approach is to rely on a high thermal conductivity matrix such as copper or silver and to improve its compliance by forming porous sponge-like structures [31-33] or arrays of nano/micro-pillars [34, 35], which typically have the ratio of thermal conductivity to effective hardness values in range of 5×10^{-8} to 3×10^{-7} m^2/K-s. However, in these cases, the increased surface area tends to cause an increased rate of oxidation and corrosion. In addition, the surface pores of metal sponge can contribute to the effective roughness, thereby adversely influencing the quality of the contact and the transport of heat.

In this study, we report a new class of thermal interface material involving metal nanocrystals coordinated with organic ligands grafted on BN nanosheets in the form of mesoscale metal-organic framework. Furthermore, this work also investigates the influence of organic ligand (linker) chemistry on the thermal and mechanical properties of the resultant material. Here, BNNS was particularly focused on because of its ultrahigh thermal conductivity, high chemical stability, and electrical insulation property [36]. In addition, Novoselov and co-workers [37] reported that some

metals can induce etching of graphene. Hence, graphene was avoided as filler although it has a higher thermal conductivity than BNNS. Silver is a metal with the second highest k/H (after indium) ratio excluding group I metals, which are highly reactive. Silver also has much higher corrosion resistivity than indium.

Regarding the ligands forming organic networks and links across the developed metal-base hybrid nanocomposites, prior studies have revealed that acyl chloride (COCl) and amino groups can react with BN nanomaterials at high yield via nucleophilic addition/elimination [38]. In this reaction, after the lone pair on the amino groups of BN performs a nucleophilic attack on the carbonyl carbon, carbonyl group reforms by releasing a chloride ion and the charge neutrality is finally achieved by deprotonation with the aid of the chloride ion. Similar to acyl chlorides, the reactions of carboxyl acid groups with BN nanomaterials were observed to occur [39]. Hence, to functionalize BN nanosheets, we selected to use three different ligands as a linker molecule between silver nano-/micro-crystals and BN nanosheets: 4-bromo-benzoyl chloride (BBC), 4-cyano-benzoyl chloride (CBC), and 2-mercapto-5-benzimidazole carboxylic acid (MBCA). With this combination, we fixed the reactive group of the ligand that directly binds to BN nanosheets (forming an amide for all cases) while changing the terminal end of the functionalized nanosheets from bromo- to cyano- to mercapto-group, thereby varying the binding strength of functionalized-BNNS to the silver matrix.

2. Materials and Methods

2.1 Materials

Materials. 4-bromo-benzoyl chloride (BBC), 4-cyano-benzoyl chloride (CBC) and 2-mercapto-5-benzimidazole carboxylic acid (MBCA) were obtained from TCI Chemicals (Philadelphia, PA, USA). Ethanol was procured from VWR (Houston, TX, USA). BNNS was purchased from M.K. Impex Corp (Mississauga, Ontario, Canada). Silver cyanide, AgCN; potassium cyanide, KCN; and potassium dicyanoargenate, $AgK(CN)_2$, which were used in the electrodeposition solution, were purchased from Sigma Aldrich (St. Louis, MO, USA).

2.2 Functionalization of BNNS

For all ligands, functionalization of BNNS was carried out in a similar fashion as described by Zhi et al. [39] Briefly, a mixture of BNNS and organic ligand at a weight ratio of 1:4 was placed in a flask equipped with a condenser. Under a nitrogen environment, the reaction content was constantly stirred using a magnetic stirrer at 120 $^{\circ}$C for 120 hours. Upon the completion of the reaction, the mixture was allowed to cool down to room temperature prior to washing in excess ethanol to get rid of the unreacted ligands. Finally, the washed product was centrifuged at 4000 rpm for 5 minutes and the precipitate was collected after drying overnight with nitrogen at 60 ^{O}C.

2.3 Characterization of Functionalization Reaction

Purified and dried products of the functionalization reaction were analyzed with an attenuated total reflectance Fourier-transform infrared spectrometer (ATR-FTIR, Shimadzu Scientific Instruments Inc., Columbia, MD). Data were acquired in the transmission mode with a resolution of 1 cm^{-1} wavenumber and are an average of 12 measurements for each ligand. Spectra were analyzed using IRsolution software package (Shimadzu).

2.4 Preparation of Thermal Interface Materials

To form hybrid metal-matrix nanocomposites, we developed an approach coupling a coordination-driven assembly and an electrodeposition process (**Fig. 1**). The key concept is that as silver nanoclusters form and deposit on the cathode through electrolytic reduction, the organic ligands on nanosheet spacers reaches to the vicinity of nanoclusters through diffusion and coordinate their assembly. The electrodeposition process was achieved using an electrolyte mixture involving 5 g of KCN, 3 g of AgCN, and 1 g of $AgK(CN)_2$ in 100 ml Milli-Q water. For the coordination reaction, one of the three ligands affixed on BNNS was used: 4-bromo-benzoyl chloride, 4-cyano-benzoyl chloride, or 2-mercapto-5-benzimidazole carboxylic acid, all of which had been grafted on BN nanosheets via Lewis acid-base reaction as described in the previous section. To achieve a net nanosheet loading of 10±1 wt.% in the nanocomposite, functionalized BNNS (i.e. nanosheet grafted with ligands) at a concentration of 0.5 wt.%-1.5 wt.% were added into the electrodeposition solution and sonicated for 30 minutes. A pure silver (>99%) and an aluminum substrate were connected to anode and cathode, respectively. The material was deposited on the aluminum substrate via pulsating electrodeposition using Powerstat05 Potentiostat (Movant Systems Inc., Crown Point, IN). The electrodeposition was carried out at a current density of 0 to 12 A/dm^2 and AC frequency of 950 Hz with 30% off time. The resultant TIMs were detached from the Al substrate, rinsed with water, dried and stored under nitrogen for further characterization.

2.5 Chemical and Structural Analysis of Nanocomposite TIMs

The obtained TIMs were cut into 1 cm × 1 cm pieces and characterized using an Omicron x-ray photoelectron spectroscopy/ultraviolet photoelectron spectroscopy (XPS/UPS) system with an Argus detector relying on dual Mg/Al X-ray source with a source energy of 1253.6 eV (Scienta Omicron GmbH, Taunusstein, Germany) to determine if a reaction between the silver crystal

matrix and functionalized nanosheets took place. Measurements involved an initial survey scan with a step size of 1.0 eV in the range of 0-1200 eV and high-resolution scans of Ag 3 $d_{5/2}$ region with a step size of 0.05 eV in the range of 362-372 eV. All spectra were corrected to the reference binding energy of ambient carbon (C 1s) at 284.8 eV. The peaks were assigned based on the NIST XPS spectra database.

The internal nanostructure of the prepared nanocomposites was examined by secondary electron microscopy (FE-SEM, JSM-7500F; JEOL, Tokyo, Japan).

2.6 Characterization of Thermal Properties of TIMs

A differential scanning calorimeter (DSC, Q20, TA Instruments, New Castle, DE) was used to measure the specific heat capacity of the samples in the modulation mode [40]. In these experiments, first, small pieces of hybrid nanocomposites were weighted with an accuracy of 0.01 mg and placed and sealed in aluminum pans. Then, the stability of the instrument was checked by monitoring DSC baseline over three cycles using blank pans. Next, the samples were mounted into the DSC chamber, which was followed by the application of a heating profile involving a combination of a sinusoidal oscillation with an amplitude of 0.5 °C and a linear ramp with a heating rate of 5 °C/min in the temperature range of 25-75 °C. Finally, the slope of the graph plotting the total heat flow (dQ/dt) versus heating rate was used to determine the heat capacity of samples at the desired temperature.

Thermal diffusivity measurements were performed via a DLF-1200 Laser Flash Diffusivity System (TA Instruments, New Castle, DE) [41]. This system relies on a Class 1 Nd:Glass Laser source to generate a collimated energy pulse with 15 J energy and 300–400 μs pulse width. In

these experiments, TIM coupons were cut into circles using a 1-inch hole punch and placed into the DLF system. Then, the front of the sample was irradiated with the laser beam while the thermal response of the rear face of the sample was monitored using a liquid nitrogen-cooled, indium antimonide IR detector. The time-temperature history of the rear face was analyzed to determine the time for the thermogram to reach the half of the maximal temperature increase, and this information was used to calculate the thermal diffusivity of the sample. The density of samples was determined via Archimedes principle.

Thermal interface resistance was measured using the phase-sensitive transient thermoreflectance (PSTTR) technique [42]. For these experiments, the samples were prepared by direct co-electrodeposition/chemisorption of TIM on silicon substrates that had previously been coated with a thin layer of chromium/silver (5nm/95nm) via electron-beam deposition. Then, a pure aluminum foil of 4.5 μm thickness was melted on top of another silicon substrate under an argon atmosphere and rapidly transferred on top of the TIM surface that was deposited on the other silicon substrate. The whole configuration was cooled to room temperature to obtain diffusive-bonded samples. The sandwiched samples were characterized using our PSTTR setup utilizing a diode pump laser with a spot diameter of 3 mm. The absorption of this energy on the front side generates a thermal wave traveling through the sample, inducing temperature fluctuation of the same frequency on the back surface. The reflectance of the surface on the back side of the sample, which is proportional to the surface temperature, was measured using a continuous wave probe laser. The comparison of the probe laser signal with the original modulation from the waveform generator, which was achieved using a photodiode and lock-in amplifier, allowed us to extract the phase shift. Through a multi-

parameter regression analysis of the phase-shift data, the bulk thermal property of different layers and the contact resistance between the layers in the sandwiched film were obtained [42].

2.7 Characterization of Mechanical Properties of TIMs

Hardness and reduced elastic modulus values were measured via a Hysitron TI 950 Triboindenter (Hysitron Inc., Minneapolis, MN). A Berkovich tip with a well-defined geometry was used for indentation and forty measurements were taken from each sample for statistical analysis as described elsewhere [43]. For each measurement, a force of 5000 mN was applied over 10 seconds, and the tip was withdrawn from the surface for 10 seconds with a 5-second holding time in between. The force versus depth curves were fitted to give the values of reduced modulus and hardness.

3. RESULT AND DISCUSSION

3.1 Functionalization of BN Nanosheets

Via nucleophilic substitution reaction, boron nitride nanosheets were functionalized with one of three different bifunctional ligands (linkers), all of which involve a terminal-end reactive towards BNNS, a benzene ring (spacer), and another terminal-end with varying affinity towards silver (Fig. 2). The functionalization reactions were characterized via the FTIR spectroscopy, the spectra of which are shown in Figure 3a for pure BN nanosheets, pure MBCA, and MBCA-functionalized BN nanosheets. The most notable difference between the spectra of pure MBCA and MBCA-BNNS is the shift of the peak from 1724 cm^{-1} to 1628 cm^{-1}, indicating a different level of coupling between the carbonyl groups and the molecular group next to it and suggesting a change from a carboxylic acid group to an amide group. In addition, no peak shift at 763 cm^{-1} and 2357 cm^{-1}

indicates that C=S (thio urea) and SH (thiolate form) terminal-edges did not react with BNNS and faced outwards from the BNNS surface. Based on these observations, a condensation reaction is proposed as illustrated in Figure 3d.

The comparison of the FTIR spectra of pure CBC and CBC-functionalized BNNS revealed that there is a peak shift from 1740 cm^{-1} to 1680 cm^{-1} after the functionalization reaction, suggesting that the carbonyl chloride group of CBC was converted into an amide group (Fig. 3b). In addition, it can be concluded that cyano-group faces away from the BNNS surface given that the peak at 2330 cm^{-1} corresponding to the cyano group is unchanged upon the functionalization reaction (Fig. 3e). Similarly, for BBC, the peak at 1766 cm^{-1} shifted to 1651 cm^{-1} indicating the conversion of carbonyl chloride in pure BBC to amide of BBC-BNNS (Fig. 3c). Likewise, the unchanged peak at 636 cm^{-1} corresponding to C-Br implies no vibrational coupling between Br and BNNS. Overall, all of the linkers formed an amide upon reacting with BNNS via their carboxylic acid or acyl chloride group, but formed functionalized BN nanosheets with a different terminal group (i.e., mercapto, cyano, or bromo) facing away from BNNS surfaces.

3.2 Formation and Chemical Analysis of Hybrid TIMs

Hybrid TIMs were prepared using a co-electrodeposition/chemisorption approach where the electrolytic reduction of silver ions into silver nano-/micro-crystals was coupled with the conjugation of ligand-coated nanosheets onto silver crystals (Fig. 1). Using this approach, four different nanocomposites involving silver as the base matrix were prepared: silver matrix with bare BNNS, BBC-functionalized BNNS, CBC-functionalized BNNS, and MBCA-functionalized BNNS. The resultant TIMs were analyzed using XPS spectroscopy, which revealed that MBCA- and CBC-functionalized BNNSs interact chemically with silver as evidenced by the positive 0.3

eV shifts in Ag $3d_{5/2}$ peak for silver-CBC-BNNS and silver-MBCA-BNNS nanocomposites (Fig. 4). These shifts can presumably be ascribed to the coordination bond between cyano and thiol groups causing silver to assume a partial positive charge due to the electron donation and cyano and thiol groups to acquire a slightly negative charge owing to the electron withdrawal. On the other hand, no chemical interaction between silver and bare BNNS or BBC-BNNS was observed.

3.3 Morphological, Thermal and Mechanical Properties of Hybrid TIMs

Upon determining the nature of chemical interactions between building blocks of metal-organic-inorganic nanocomposites, morphological (nanostructure), thermal and mechanical properties were investigated. Secondary electron microscopy (SEM) imaging of fractured samples provided insights into the organization and distribution of BN nanosheets in silver crystal matrix as a function of ligand (linker) chemistry (Fig. 5). Bare BNNS and BBC-functionalized BNNS aggregated and strongly phase-separated from the silver-base matrix, which can be attributed to the interfacial energy mismatch between BN and silver (Fig. 5b&c). On the other hand, for the cases of CBC-functionalized and MBCA-functionalized BN nanosheets, the distribution of nanosheets within the matrix was more uniform while some aggregation was still observed (Fig. 5d&e). These observations support the idea that the chemical interactions between functionalized BNNS and ligands improve the integrity of metal-inorganic-organic hybrid nanocomposites. These findings are also consistent with the XPS data in that CBC-functionalized and MBCA-functionalized BN nanosheets react with Ag while no reaction occurred between silver and bare BNNS and BBC-functionalized BNNS.

The presence and nature of the organic linker influences the thermal conductivity of nanocomposite TIMs (Figure 6a). For a fixed filler volume fraction of 10±1 wt.%, the effective

thermal conductivity of chemically-integrated nanocomposites (i.e. the filler is CBC-BNNS or MBCA-BNNS) was about 25-40% higher than that of physically-integrated nanocomposites (i.e. the filler is BBC-BNNS). However, regardless of the functionalization state of BNNS, the introduction of BNNS into silver matrix resulted in a reduction of the effective thermal conductivity in comparison to pure silver, which can be explained by the out-of-plane thermal conductivity of BNNS being lower than that of pure silver, and the relatively low thermal conductivity of organic linkers. The effective thermal conductivity of chemically-linked nanocomposites was significantly larger than that of physically-linked nanocomposites (306-321 W/m-K versus 236-258 W/m-K. Since the thermal transport is primarily due to the transport of electrons, we also compared the electrical conductivities of these TIM nanocomposites (Table 1.) It was found that the electrical conductivity trends followed the thermal conductivity trends i.e., pure silver is the highest, followed by the chemically functionalized nanocomposites, and nanocomposites with physically trapped BNNS being the lowest. These consistent trend is consistent with the Wiedemann-Franz law and can explain the observed variations in thermal conductivities [44].

Table 1. The comparison of electrical conductivity of various types of composite TIMs at 25 °C.

Material	Electrical Conductivity	
	Average (S/m)	Standard Deviation (S/m)
Pure Ag	6.1×10^{7}	5.7×10^{2}
Ag- pure BNNS	1.1×10^{5}	7.8×10^{2}
Ag- BBC-BNNS	9.7×10^{4}	5.6×10^{2}
Ag- CBC-BNNS	1.5×10^{5}	9.2×10^{2}
Ag-MBCA-BNNS	1.9×10^{5}	7.9×10^{2}

Figure 6b shows the reduced modulus and hardness of these nanocomposites obtained using nanoindentation. Silver-based nanocomposites were found to be softer and more compliant than pure silver. This trend is presumably because the presence of BNNS and functionalized-BNNS disrupts metallic bonds between silver crystals within the film and in addition, will reduce the van der Waals interactions between silver crystals considering that the dielectric constant of metals is much higher than that of inorganic and organic materials. Furthermore, the occupation of f-BNNSs at grain boundaries may promote the slippage of metallic interface, which softens nanocomposites [45, 46]. Furthermore, the ligand molecules act as cushions due to their inherent softness.

The hardness and modulus values of chemically integrated nanocomposites were lower than that of physically integrated nanocomposites, which is counter-intuitive considering only the types and strengths of the bonds involved. However, physically integrated nanocomposites experience the aggregation of fillers as shown in Figure 5. For a given nominal filler loading, the existence of the regions containing BNNS aggregates reduces the effective concentration of BNNS in the regions without BNNS aggregates due to the availability of lower amount of fillers on average. Namely, the effective filler concentration is reduced in the regions where there is no aggregation. Assuming the mechanical properties of fillers do not change significantly with aggregation, the effective medium theory can explain the observed trends [47,48].

Based on the measured thermomechanical properties, the k/H ratio for these silver-based nanocomposites is calculated to be 1.3×10^{-6} m^2/K-s for the case of MBCA-BNNS fillers and 8.5×10^{-7} m^2/K-s for the case of CBC-BNNS fillers. Considering pure silver samples prepared had a k/H ratio of 3.9×10^{-7} m^2/K-s, these values signify noticeable improvements (118% to 233% improvement) in thermomechanical properties of chemically integrated nanocomposites. On the

other hand, the physically integrated nanocomposites yielded a k/H ratio of 5.2×10^{-7}–5.9×10^{-7} m^2/K-s. Using the PSTTR technique, a thermal interface resistance of 0.05±0.02 mm^2.K/W and 0.06±0.02 mm^2.K/W was measured at the Si-TIM interface under adhesive loading for nanocomposites with chemisorbed and physisorbed fillers, respectively in comparison to 0.12±0.03 mm^2.K/W for the case of pure silver (**Table 2**). Results from pure silver, nanocomposite with physisorbed fillers and chemisorbed fillers are summarized in Table 1. The contact thermal resistance of the nanocomposite materials is measured to be lower than that of the silver. This trend may be attributed to potentially reduced number of defects at the interface due to the increased interfacial energy compatibility between Si and Ag with the addition of organic ligands [49-51]. Combining the thermal resistances from both bulk material and surface contact, the overall thermal resistance when the hybrid nanocomposite is used as TIM is calculated to be around 0.35 mm^2·K/W, more than two orders of magnitude lower than common commercial TIM products.

Table 2. The thermal interface resistance and total resistance of nanocomposite TIMs directly chemisorption-coupled electrodeposited on molecular smooth silicon wafer.

	Si-TIM interface resistance (mm^2·K/W)	Overall thermal resistance (mm^2·K/W)
Pure silver	0.12 ± 0.04	0.27 ± 0.04
Nanocomposite with physisorbed fillers	0.05	0.34
Nanocomposite with chemisorbed fillers	0.06	0.35

To determine the influence of temperature on the thermal properties of these TIM, we used laser flash analysis (Table 3). It was found that thermal conductivity of composites involving physical bonding of BNNS and silver did not change significantly with temperature while there was a small increase in thermal conductivity of composites involving chemical bonding of BNNS and silver.

Table 3. The comparison of thermal conductivity of various types of composite TIMs at 25 °C and 250 °C.

	K (W/m-K) 25 °C	K (W/m-K) 250 °C
Pure Ag	374±5	372±8
Ag/pure BNNS	258±21	261±7
Ag/BBC-BNNS	236±16	230±3
Ag/CBC-BNNS	306±41	354±8
Ag/MBCA-BNNS	321±68	382±6

4. Conclusions

Overall, this work has three key conclusions, important in the context of materials science, thermal management, and nanotechnology. First, using the coordination chemistry in conjunction with an electrodeposition process, it is possible to fabricate chemically-linked hybrid nanocomposites involving a silver matrix, 2-D BN nanosheets, and organic ligands. Second, the nanostructure, thermal and mechanical properties of these hybrid nanocomposites strongly depend on the chemistry of linker molecules (ligands) physically or chemically binding nanosheets to the silver matrix. BN nanosheets with cyano- and thio- terminal groups are uniformly distributed in the silver matrix while bare BN nanosheets and BN nanosheets with bromo- terminal groups are in a strongly aggregated state in the silver matrix. The thermal transport in thio- and cyano-linked nanocomposites of silver and BN nanosheets is more efficient than that in bromo-linked nanocomposites. This difference is presumably due to the increased electrical conductivity in the presence of chemical bonds in comparison to the physical bonds. Third, while the presence of bare and functionalized BN nanosheets somewhat reduced the thermal conductivity of pure silver, the mechanical compliance and deformability of nanocomposites were significantly better than pure silver. To put the improvement in mechanical compliance relative to the loss of thermal conductivity in perspective, we determined the thermal conductivity-to-hardness ratio (k/H ratio), which is a critical metric controlling the thermal interface resistance, and found that chemically-integrated nanocomposites improves this ratio from 3.9×10^{-7} m^2/K-s (pure silver) to $1.3x10^{-6}$–$8.5x10^{-7}$ m^2/K-s, (i.e. ~118% to ~233% enhancement in comparison to pure silver). With such intriguing thermomechanical properties and scalable methodology of production, these

nanomaterials can be applied in various thermal management systems to relieve the thermal stresses in next generation devices and applications.

Author Information

Corresponding Author: Mustafa Akbulut, e-mail: makbulut@tamu.edu

Funding Sources

NSF Grant 1559627, DARPA Award No: D13AP00040, and DARPA IAG-12-1844

Acknowledgement

This research was developed with funding from the Defense Advanced Research Projects Agency (DARPA). The views, opinions and/or findings expressed are those of the authors and should not be interpreted as representing the official views or policies of the Department of Defense or the U.S. Government. M.A acknowledges funding from NSF Grant 1559627 and DARPA Award No: D13AP00040. X.F., C.K., and S.N. acknowledge funding from DARPA through the Interagency Agreement IAG-12-1844.

References

[1] J.A. Mason, J. Oktawiec, M.K. Taylor, M.R. Hudson, J. Rodriguez, J.E. Bachman, M.I. Gonzalez, A. Cervellino, A. Guagliardi, C.M. Brown, P.L. Llewellyn, N. Masciocchi, J.R. Long, Methane storage in flexible metal–organic frameworks with intrinsic thermal management, Nature. 527 (2015) 5–7.

[2] H. Huang, C. Liu, Y. Wu, S. Fan, Aligned carbon nanotube composite films for thermal management, Adv. Mater. 17 (2005) 1652–1656.

[3] Z. Yan, G. Liu, J.M. Khan, A. a. Balandin, Graphene quilts for thermal management of high-power GaN transistors, Nat. Commun. 3 (2012) 827.

[4] J. Chen, X. Huang, Y. Zhu, P. Jiang, Cellulose Nanofiber Supported 3D Interconnected BN Nanosheets for Epoxy Nanocomposites with Ultrahigh Thermal Management Capability, Adv. Funct. Mater. 27 (2017) 1–9.

[5] A. Balčytis, M. Ryu, G. Seniutinas, P.R. Stoddart, M.A. Al Mamun, J. Morikawa, S. Juodkazis, Nano-rescaling of gold films on polystyrene: thermal management for SERS, Nanoscale. 9 (2016) 690–695.

[6] N. Song, D. Jiao, S. Cui, X. Hou, P. Ding, L. Shi, Highly Anisotropic Thermal Conductivity of Layer-by-Layer Assembled Nanofibrillated Cellulose/Graphene Nanosheets Hybrid Films for Thermal Management, ACS Appl. Mater. Interfaces. 9 (2017) 2924–2932.

[7] S. Kwon, J. Zheng, M.C. Wingert, S. Cui, R. Chen, Unusually High and Anisotropic Thermal Conductivity in Amorphous Silicon Nanostructures, ACS Nano. 11 (2017) 2470–2476.

[8] F.E. Alam, W. Dai, M. Yang, S. Du, X. Li, J. Yu, N. Jiang, C.-T. Lin, In situ formation of a cellular graphene framework in thermoplastic composites leading to superior thermal conductivity, J. Mater. Chem. A. 5 (2017) 6164–6169.

[9] J. Hu, Y. Huang, Y. Yao, G. Pan, J. Sun, X. Zeng, R. Sun, J. Bin Xu, B. Song, C.P. Wong, Polymer Composite with Improved Thermal Conductivity by Constructing a Hierarchically Ordered Three-Dimensional Interconnected Network of BN, ACS Appl. Mater. Interfaces. 9 (2017) 13544–13553.

[10] Y. Wang, N. Xu, D. Li, J. Zhu, Thermal Properties of Two Dimensional Layered Materials, Adv. Funct. Mater. 27 (2017) 1604134.

[11] J.D. van Wyk, F.C. Lee, On a Future for Power Electronics, IEEE J. Emerg. Sel. Top. Power

Electron. 1 (2013) 59–72.

[12] H.S. Hamut, I. Dincer, G.F. Naterer, Exergy analysis of a TMS (thermal management system) for range-extended EVs (electric vehicles), Energy. 46 (2012) 117–125.

[13] R. Prasher, Thermal Interface Materials: Historical Perspective, Status, and Future Directions, Proc. IEEE. 94 (2006) 1571–1586.

[14] A. Yu, P. Ramesh, X. Sun, E. Bekyarova, M.E. Itkis, R.C. Haddon, Enhanced Thermal Conductivity in a Hybrid Graphite Nanoplatelet - Carbon Nanotube Filler for Epoxy Composites, Adv. Mater. (Weinheim, Ger.). 20 (2008) 4740–4744.

[15] A. Bar-Cohen, K. Matin, S. Narumanchi, Nanothermal Interface Materials: Technology Review and Recent Results, J. Electron. Packag. 137 (2015) 40803–40817.

[16] Y. Xu, X. Luo, D.D.L. Chung, Lithium Doped Polyethylene- Glycol-Based Thermal Interface Pastes for High Thermal Contact Conductance, J. Electron. Packag. 122 (2000) 188–191.

[17] S. Stankovich, D. a Dikin, G.H.B. Dommett, K.M. Kohlhaas, E.J. Zimney, E. a Stach, R.D. Piner, S.T. Nguyen, R.S. Ruoff, Graphene-based composite materials., Nature. 442 (2006) 282–286.

[18] V. Goyal, A.A. Balandin, Thermal properties of the hybrid graphene-metal nano-micro-composites: Applications in thermal interface materials, Appl. Phys. Lett. 100 (2012) 073113.

[19] E.G. Wolff, D.A. Schneider, Prediction of thermal contact resistance between polished surfaces, Int. J. Heat Mass Transf. 41 (1998) 3469–3482.

[20] V. Sartre, M. Lallemand, Enhancement of thermal contact conductance for electronic

systems, Appl. Therm. Eng. 21 (2001) 221–235.

[21] R.L. Jackson, S.H. Bhavnani, T.P. Ferguson, A Multiscale Model of Thermal Contact Resistance Between Rough Surfaces, J. Heat Transfer. 130 (2008) 81301.

[22] M.M. Yovanovich, Four decades of research on thermal contact, gap, and joint resistance in microelectronics, IEEE Trans. Compon., Packag., Manuf. Technol. 28 (2005) 182–206.

[23] S. Wang, Y. Cheng, R. Wang, J. Sun, L. Gao, Highly thermal conductive copper nanowire composites with ultralow loading: Toward applications as thermal interface materials, ACS Appl. Mater. Interfaces. 6 (2014) 6481–6486.

[24] J.S. Park, Y.J. An, K. Shin, J.H. Han, C.S. Lee, Enhanced thermal conductivity of epoxy/three-dimensional carbon hybrid filler composites for effective heat dissipation, RSC Adv. 5 (2015) 46989–46996.

[25] G. Lian, C.-C. Tuan, L. Li, S. Jiao, Q. Wang, K.-S. Moon, D. Cui, C.-P. Wong, Vertically Aligned and Interconnected Graphene Networks for High Thermal Conductivity of Epoxy Composites with Ultralow Loading, Chem. Mater. 28 (2016) 6096–6104.

[26] Y. Yao, X. Zeng, G. Pan, J. Sun, J. Hu, Y. Huang, R. Sun, J.-B. Xu, C.-P. Wong, Interfacial Engineering of Silicon Carbide Nanowire/Cellulose Microcrystal Paper toward High Thermal Conductivity, ACS Appl. Mater. Interfaces. 8 (2016) 31248–31255.

[27] T. Eyassu, T.-J. Hsiao, K. Henderson, T. Kim, C.-T. Lin, Molecular Cooling Fan: Factors for Optimization of Heat Dissipation Devices and Applications, Ind. Eng. Chem. Res. 53 (2014) 19550–19558.

[28] Q. Li, Y. Guo, W. Li, S. Qiu, C. Zhu, X. Wei, M. Chen, C. Liu, S. Liao, Y. Gong, Ultrahigh thermal conductivity of assembled aligned multilayer graphene/epoxy composite, Chem.

Mater. 26 (2014) 4459–4465.

[29] X. Fang, L.-W. Fan, Q. Ding, X. Wang, X.-L. Yao, J.-F. Hou, Z.-T. Yu, G.-H. Cheng, Y.-C. Hu, K.-F. Cen, Increased thermal conductivity of eicosane-based composite phase change materials in the presence of graphene nanoplatelets, Energy Fuels. 27 (2013) 4041–4047.

[30] M. Shtein, R. Nadiv, M. Buzaglo, K. Kahil, O. Regev, Thermally conductive graphene-polymer composites: size, percolation and synergy effects, Chem. Mater. 27 (2015) 2100-2106.

[31] P.-C. Hsu, X. Liu, C. Liu, X. Xie, H.R. Lee, A.J. Welch, T. Zhao, Y. Cui, Personal thermal management by metallic nanowire-coated textile, Nano Lett. 15 (2014) 365–371.

[32] B. Wunderle, M. Klein, L. Dietrich, M. Abo Ras, R. Mrossko, D. May, R. Schacht, H. Oppermann, B. Michel, H. Reichl, Advances in thermal interface technology: Mono-metal interconnect formation, processing and characterisation, ITherm 2010, Intersoc. Conf. Therm. Thermomech. Phenom. Electron. Syst., 12th. (2010) 1-10.

[33] X. Gui, J. Wei, K. Wang, A. Cao, H. Zhu, Y. Jia, Q. Shu, D. Wu, Carbon nanotube sponges, Adv. Mater. (Weinheim, Ger.) 22 (2010) 617–621.

[34] M. Qin, Y. Feng, T. Ji, W. Feng, Enhancement of cross-plane thermal conductivity and mechanical strength via vertical aligned carbon nanotube@graphite architecture, Carbon. 104 (2016) 157–168.

[35] R. Sasaki, K. Shintani, Hardness of Pillared-Graphene Nanostructures via Indentation Simulation, MRS Adv. 2 (2017) 45–50.

[36] D. Golberg, Y. Bando, Y. Huang, T. Terao, M. Mitome, C. Tang, C. Zhi, Boron nitride

nanotubes and nanosheets, ACS Nano. 4 (2010) 2979–2993.

[37] Q.M. Ramasse, R. Zan, U. Bangert, D.W. Boukhvalov, Y.-W. Son, K.S. Novoselov, Direct experimental evidence of metal-mediated etching of suspended graphene, ACS Nano. 6 (2012) 4063–4071.

[38] J. Chen, M. Hamon, H. Hu, Y. Chen, A. Rao, P. Eklund, R. Haddon, Solution properties of single-walled carbon nanotubes, Science. 282 (1998) 95–98.

[39] C. Zhi, Y. Bando, C. Tang, S. Honda, K. Sato, H. Kuwahara, D. Golberg, Covalent functionalization: towards soluble multiwalled boron nitride nanotubes., Angew. Chem. Int. Ed. 44 (2005) 7932–7935.

[40] P.S. Gill, S.R. Sauerbrunn, M. Reading, Modulated differential scanning calorimetry, J. Therm. Anal. 40 (1993) 931–939.

[41] H.W. Deem, W.D. Wood, Flash thermal-diffusivity measurements using a laser, Rev. Sci. Instrum. 33 (1962) 1107–1109.

[42] X. Feng, C. King, D. Devoto, M. Mihalic, S. Narumanchi, Investigation of thermal interface materials using phase-sensitive transient thermoreflectance technique, ITherm 2014, Intersoc. Conf. Therm. Thermomech. Phenom. Electron. Syst., 14th. (2014) 1296–1307.

[43] C. Yegin, N. Nagabandi, X. Feng, C. King, M. Catalano, J.K. Oh, A. Talib, E.A. Scholar, S. V. Verkhoturov, T. Cagin, A. V. Sokolov, M.J. Kim, K. Matin, S. Narumanchi, M. Akbulut, Metal-Organic-Inorganic Nanocomposite Thermal Interface Materials with Ultra-Low Thermal Resistances, ACS Appl. Mater. Interfaces. 9 (2017) 10120–10127.

[44] Wilson, R.B. and Cahill, D.G., 2012. Experimental validation of the interfacial form of the Wiedemann-Franz law. Physical review letters, 108(25), p.255901.

[45] Broedling, N.C., Hartmaier, A., Buehler, M.J. and Gao, H., 2008. The strength limit in a bio-inspired metallic nanocomposite. Journal of the Mechanics and Physics of Solids, 56(3), pp.1086-1104.

[46] Sofronis, P. and McMeeking, R.M., 1994. The effect of interface diffusion and slip on the creep resistance of particulate composite materials. Mechanics of materials, 18(1), pp.55-68.

[47] J.C. Halpin, J.L. Kardos, The Halpin-Tsai equations: A review, Polym. Eng. Sci. 16 (1976) 344–352.

[48] M.A. Rafiee, J. Rafiee, Z. Wang, H. Song, Z.Z. Yu, N. Koratkar, Enhanced mechanical properties of nanocomposites at low graphene content, ACS Nano. 3 (2009) 3884–3890.

[49] Van Loenen, E.J., Iwami, M., Tromp, R.M. and Van der Veen, J.F., 1984. The adsorption of Ag on the Si (111) 7× 7 surface at room temperature studied by medium energy ion scattering, LEED and AES. Surface science, 137(1), pp.1-22.

[50] Guerin, D., Merckling, C., Lenfant, S., Wallart, X., Pleutin, S. and Vuillaume, D., 2007. Silicon− Molecules− Metal Junctions by Transfer Printing: Chemical Synthesis and Electrical Properties. The Journal of Physical Chemistry C, 111(22), pp.7947-7956.

[51] Laibinis, P.E., Whitesides, G.M., Allara, D.L., Tao, Y.T., Parikh, A.N. and Nuzzo, R.G., 1991. Comparison of the structures and wetting properties of self-assembled monolayers of n-alkanethiols on the coinage metal surfaces, copper, silver, and gold. Journal of the American Chemical Society, 113(19), pp.7152-7167.

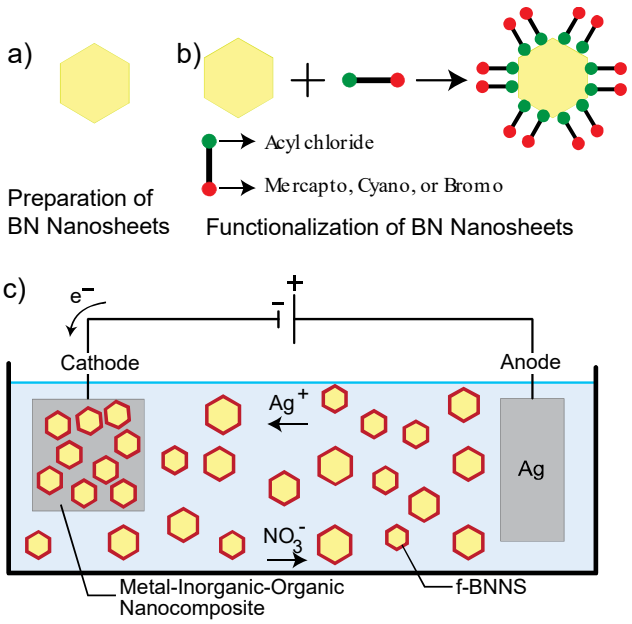

Figure 1. Three main steps of preparing hybrid nanocomposites involving silver, BN nanosheets, and organic ligands: a) the preparation of BN nanosheets via ultrahigh-intensity sonification assisted exfoliation in n-methyl-2-pyrrolidone, b) the functionalization of BN nanosheets with bifunctional ligands containing acyl chloride or carboxylic acid groups through Lewis acid-base reactions, and c) the co-electrodeposition/chemisorption process that couples the electrolytic reduction of silver ions and the chemisorption of functionalized BN nanosheets on the cathode.

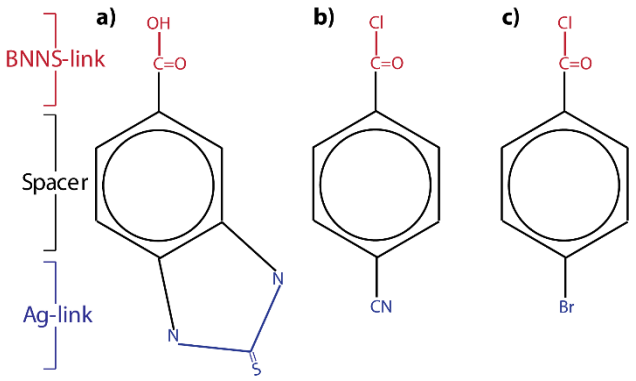

Figure 2. Generic and specific structures of selected ligands: a) 2-mercapto-5-benzimidazole carboxylic acid (MBCA), b) 4-cyanobenzoyl chloride (CBC), and c) 4-bromo-benzoyl chloride (BBC).

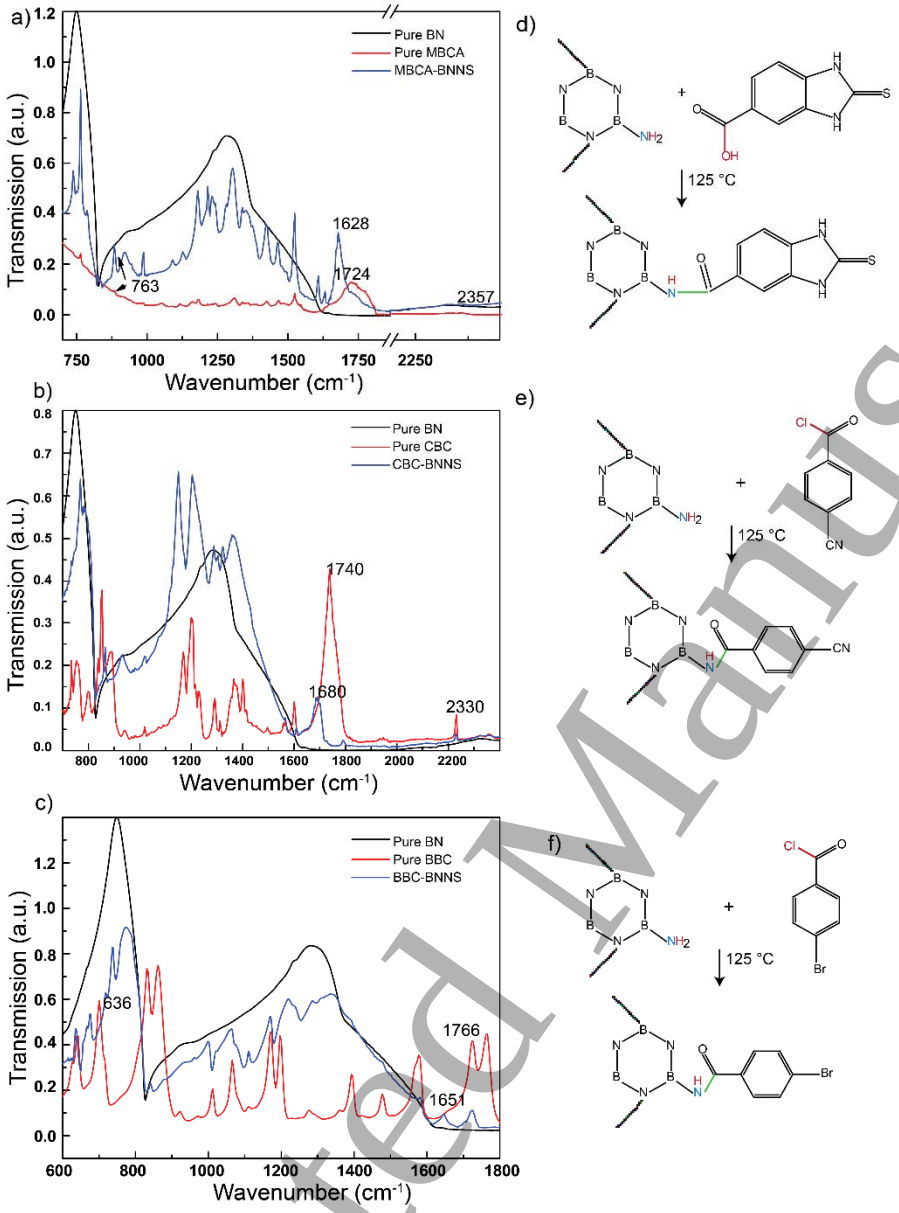

Figure 3. FTIR spectra of a) pure BNNS, pure MBCA, and MBCA-functionalized BNNS, b)pure BNNS, pure CBC, and CBC-functionalized BNNS, and c) pure BNNS, pure BBC and CBC-functionalized BNNS. The proposed reactions for the chemical interactions of d) MBCA and BNNS, e) CBC and BNNS, and f) BBC and BNNS.

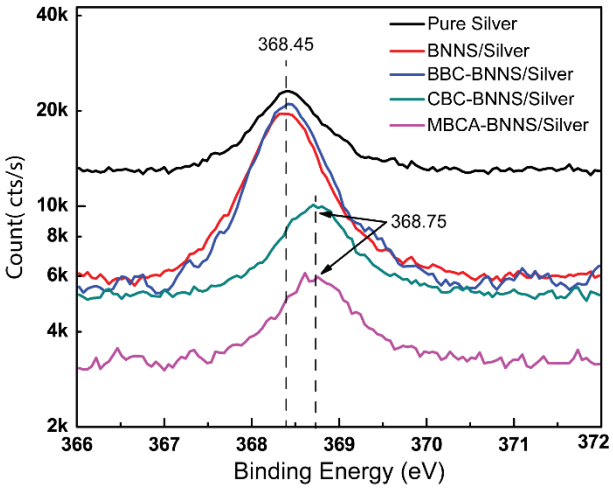

Figure 4. High resolution XPS spectra in the region of Ag 3 $d_{5/2}$ for pure silver, nanocomposites involving bare BNNS and silver, nanocomposites involving BBC-functionalized BNNS and silver, nanocomposites involving CBC-functionalized BNNS and silver, and nanocomposites involving MBCA-functionalized BNNS and silver. No peak shifts were observed for the cases of pure BNNS and BBC-BNNS compared to pure silver. Nanocomposites with CBC-BNNS or MBCA-BNNS fillers showed an oxidative shift of 0.3 eV, suggesting the chemical integration of BN nanosheets containing thio- and cyano-terminal groups with the silver matrix.

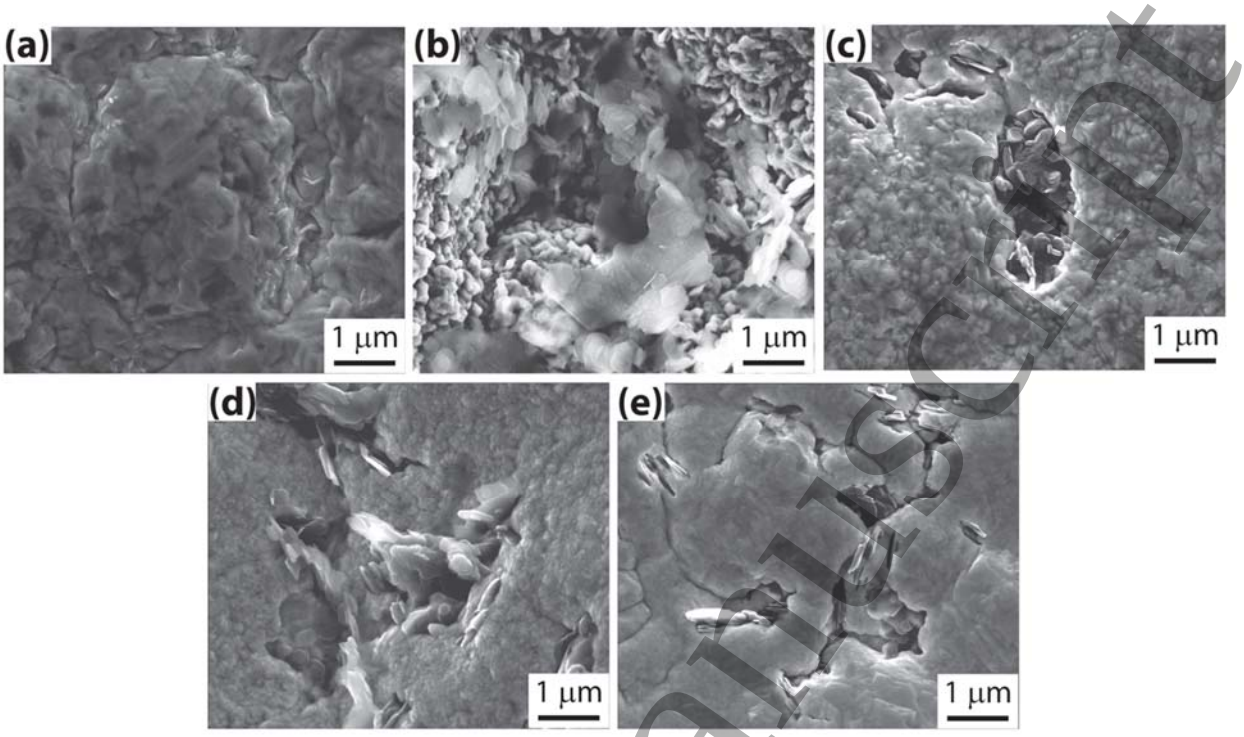

Figure 5. Secondary electron micrographs of (a) pure silver, and silver-matrix nanocomposites involving (b) bare BNNS, (c) BBC-functionalized BNNS, (d) CBC-functionalized BNNS, and (e) MBCA-functionalized BNNS. Nanocomposites with bare BNNS and BBC-functionalized BNNS showed a strong aggregation of nanosheets in the silver matrix while CBC-functionalized and MBCA-functionalized nanosheets resulted in a better dispersion and distribution of nanosheets in the matrix.

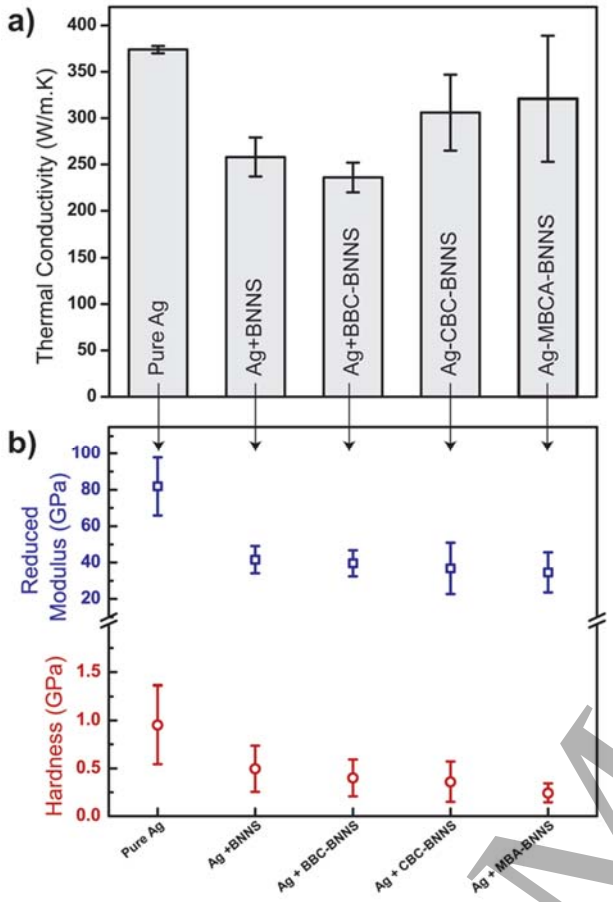

Figure 6. a) Thermal conductivity and b) reduced modulus and hardness values of chemically-integrated (CBC-BNNS and MBCA-BNNS)) and physically-integrated hybrid nanocomposites in comparison to pure silver.